CORA Cork Open Research Archive
Cartlann Taighde Oscailte Chorcaí

Title	Preferential <111>A pore propagation mechanism in n-InP anodized in KOH
Authors	Lynch, Robert P.;O'Dwyer, Colm;Quill, Nathan;Nakahara, Shohei;Newcomb, Simon B.;Buckley, D. Noel
Publication date	2008-10-01
Original Citation	Lynch, R., O'Dwyer, C., Quill, N., Nakahara, S., Newcomb, S. B. and Buckley, D. N. (2008) 'Preferential <111>A Pore Propagation Mechanism in n-InP Anodized in KOH', ECS Transactions, 16(3), pp. 393-404.
Type of publication	Article (peer-reviewed)
Link to publisher's version	http://ecst.ecsdl.org/content/16/3/393.abstract - 10.1149/1.2982579
Rights	© 2008 ECS - The Electrochemical Society
Download date	2026-11-01 14:12:36
Item downloaded from	https://hdl.handle.net/10468/6306

UCC
University College Cork, Ireland
Coláiste na hOllscoile Corcaigh

Preferential <111>A Pore Propagation Mechanism in n-InP Anodized in KOH

R. Lynch[a], C. O'Dwyer[a], N. Quill[a], S. Nakahara, S. B. Newcomb[b], and D. N. Buckley[a]

Materials and Surface Science Institute, University of Limerick, Ireland

[a] *Department of Physics, University of Limerick, Ireland*
[b] *Glebe Scientific Limited, Newport, Co. Tipperary, Ireland*

This paper describes the formation of pores during the anodization of n-InP in aqueous KOH. The pores propagate preferentially along the <111>A crystallographic directions and form truncated tetrahedral domains. A model is presented that explains preferential <111>A pore propagation and the uniform diameters of pores. The model outlines how pores can deviate from the <111>A directions and from their characteristic diameters. It also details the effect of variation of carrier concentration on the dimensions of the porous structures.

Introduction

Porosity in electrochemically etched semiconductors has been extensively investigated in the case of silicon (1) and to a lesser extent in the case of III-V compounds such as GaAs (2,3) and InP (4,5). Anion type and concentration can play a significant role in affecting the pore growth and morphology (6,7). The depth of porous layers and their preferential crystallographic growth directions have been shown to be affected by the substrate type (8), orientation (9) and doping density (10).

We have previously investigated (11,12) the early stages of anodic formation of porous InP in 5 mol dm^{-3} KOH and reported transmission electron microscopy (TEM) and scanning electron microscopy (SEM) evidence that clearly shows individual nanoporous domains. From this work we concluded that pore propagation was preferentially along the <111>A direction and that the resulting nanoporous domains that initially form have triangular $(01\bar{1})$ cross-sections, 'dove-tail' (011) cross-sections and rectangular profiles when (100) planes are viewed in parallel to the electrode surface. It was also observed by our group (13,14) that these structures are obtained when InP is anodized in KOH at concentrations of 2 mol dm^{-3} or above. Pores originating from pits in the surface create porous domains beneath a thin (~40 nm) dense near-surface layer and eventually these domains merge to create a continuous porous layer (15). However, at concentrations of 1 mol dm^{-3} or less, no porous layers were observed and between 1.8 mol dm^{-3} and 1.0 mol dm^{-3} a transition region of highly porous growth (without the presence of a near surface layer) was observed (16).

This paper describes an investigation by SEM and TEM of pore propagation in n-InP anodized in KOH and presents a model for the preferential propagation and branching of pores along the <111>A direction.

Experimental

The working electrode consisted of polished (100)-oriented monocrystalline sulfur-doped n-type indium phosphide (n-InP). An ohmic contact was made to the back of the InP

sample and isolated electrically from the electrolyte by means of a suitable varnish. The electrode area was typically 0.5 cm^2. InP wafers with carrier concentrations from 3.4-6.7 $\times 10^{18}$ cm^{-3} and etch pit densities <500 cm^{-2} were used. Anodization was carried out in aqueous KOH electrolytes of 5 mol dm^{-3}. Each experiment involved a linear potential sweep (LPS) at 2.5 mV s^{-1} from 0.0 V (SCE) to an upper potential. A conventional three-electrode cell configuration was used employing a platinum counter electrode and saturated calomel reference electrode (SCE) to which all potentials were referenced. Prior to immersion in the electrolyte, the working electrode was dipped in an etchant (3:1:1 H_2SO_4:H_2O_2:H_2O) for 4 minutes and then rinsed in deionized water. All of the electrochemical experiments were carried out in the absence of light at room temperature.

A CH Instruments Model 650A Electrochemical Workstation interfaced to a Personal Computer was employed for cell parameter control and for data acquisition. Cleaved {011} cross-sections were examined using a HITACHI S-4800 field emission SEM operating at 5 kV. Electron transparent sections for cross-sectional TEM were prepared using standard focused ion beam milling (FIB) procedures (17) in a FEI 200 FIB workstation. The TEM characterization was performed using a JEOL JEM 2010 TEM operating at 200 kV.

Results and Discussion

Cross-Sectional Microscopy

Fig. 1 shows an SEM image of a porous layer (011) cross-section. In this image, two primary pores that have grown all the way through the porous layer from a pit in the electrode surface are clearly visible.

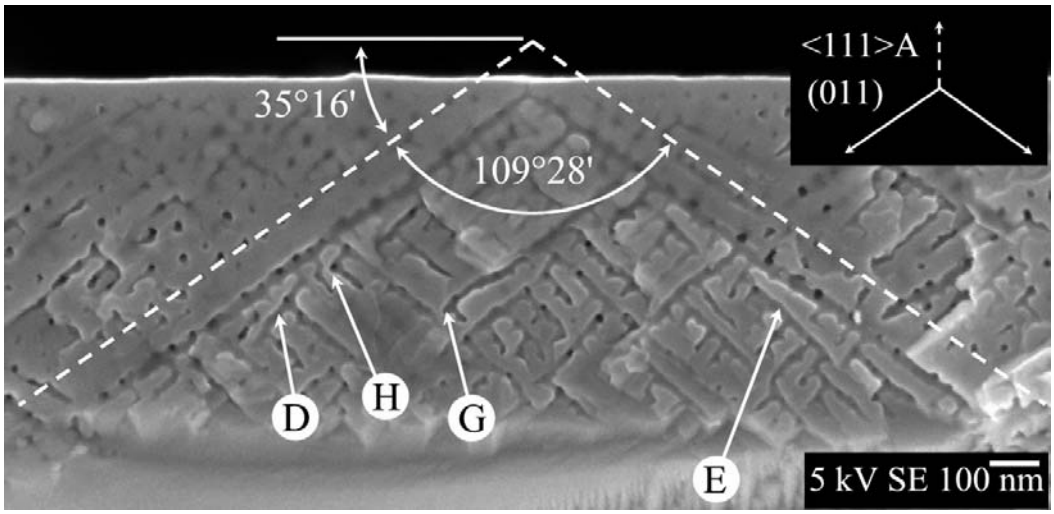


Fig. 1 Cross-sectional (011) SEM micrograph of InP following an LPS from 0 to 0.46 V (SCE) at 2.5 mV s^{-1} in 5 mol dm^{-3} KOH. The current peak in the LSV is at 0.46 V (SCE). The <111> directions are superimposed on the image as white, dotted lines. Two primary pores extending from a pit in the surface are clearly along <111>A. Pores that deviate from these directions are indicated at D and E and pores that have avoided crossing each other are indicated at G and H.

It is clear from the superimposed lines representing the <111> directions that these two primary pores have propagated preferentially along the <111>A directions.

Measurement of the pore width shows that the pore has the same width for its entire length except where it narrows near the surface pit and pore tip. Other (shorter) pores are also visible. They are generally along the <111> directions but deviate somewhat from these directions in places. Where pores are in close proximity to each other they have diverged (e.g. at D and E), and when growing towards each other they have avoided crossing (e.g. at G and H). This tendency of pores to grow around obstacles is frequently observed in micrographs and will be discussed later in the context of the proposed pore propagation model. The pores appear to have a uniform width: there is no evidence that the pores are wider closer to the surface. This suggests that pore growth occurs only at the pore tips with no subsequent widening due to etching at pore walls in the electrolyte-filled pores.

Fig. 2 shows an SEM micrograph of the cleavage plane orthogonal to that shown in Fig. 1. Also, during anodization the potential sweep was stopped at a lower potential, before the domains had time to fully merge together. Therefore, the characteristic triangular ($01\bar{1}$) cross-sections associated with these domains (11) are visible. Two types of pores are evident: those passing through the plane of the image (Type 1) and those in the plane of the image (Type 2). The Type 1 pores appear as round cross-sections in Fig. 2 and are in (011) planes (such as that in Fig. 1) orthogonal to the ($01\bar{1}$) plane of the image. Each of the Type 2 pores can be seen to have originated at a Type 1 pore and to have grown along <111>A towards the surface (*i.e.* upwards at ~35^{o} to the horizontal in Fig. 2). Where pores come close to the near-surface layer they deviate (F) from their preferred propagation direction leaving the near-surface layer intact. Indeed, most Type 2 pores in Fig. 2 deviate from the <111>A direction due to the proximity of Type 1 pores.

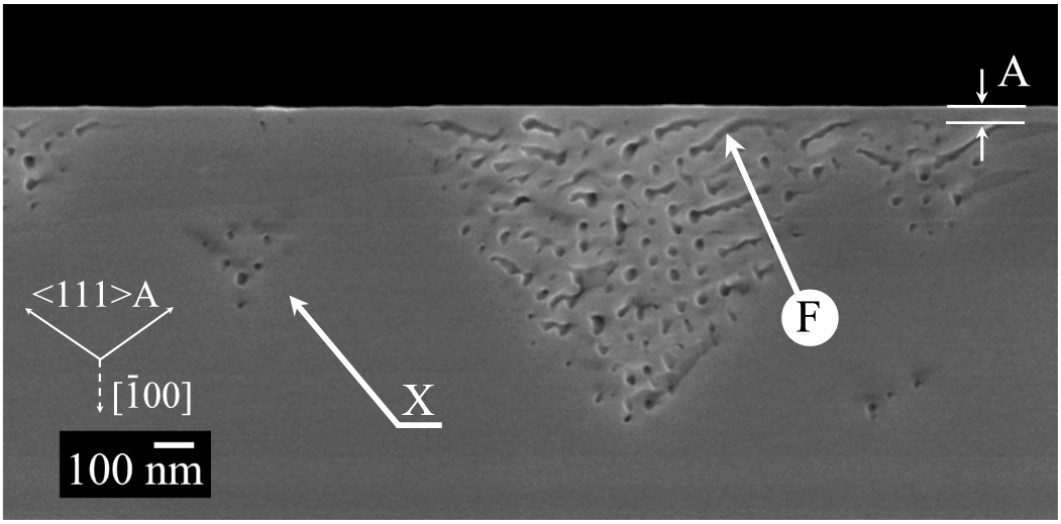


Fig. 2 Cross-sectional SEM image of InP cleaved along the ($01\bar{1}$) plane (orthogonal to Fig. 1) following an LPS from 0 to 0.44 V (SCE) at 2.5 mV s^{-1} in 5 mol dm^{-3} KOH. The pores shown in Fig. 1 (Type 1) appear as round cross-sections in this figure. The near-surface layer at A is also visible. Pores in the plane of the image (Type 2) propagate upwards at ~35^{o} to the horizontal along the <111>A directions. A pore that has deviated from <111>A as it approaches the near-surface layer is indicated at F. The apex of an adjacent domain is shown at X.

Pore Cross-Section and Tip Shape

Fig. 3 shows two TEM images where the sample has been tilted to the <111>B direction so as to observe the pore cross-sections as viewed along a pore axis. The cross-section in Fig. 3a passes close to the apex of a porous domain and intersects a pore very close to its tip (at G). The light-grey triangular area at G appears to define three facets. The sides of this triangle are approximately parallel to the intersections of the {111} planes with the image plane as shown in the inset. Thus, the internal surface of the tip of a pore appears to consist of {111}A facets (the arrows in the inset represent the <111>A directions). The cross-section shown in Fig. 3b intersects pores far from their tips. It is clear that, in contrast with Fig. 3a, these cross-sections are quasi-circular.

The observation of a uniform pore width in Fig. 1 is also consistent with the fact that no particular crystallographic facets have been observed at the pore walls; as far as can be determined, the pore cross-sections are round with no facets apparent except near the tip. If etching occurred at the pore walls as well as at the pore tip, it might be expected that the walls would be faceted, giving a characteristic pore shape such as a triangular cross-section. For example, Osaka *et al.* (18) reported that pores formed along the <100> directions during etching of silicon in HF solution had square cross-sections. However, in that case the pores were tapered, being wider close to their points of origin at the surface. This suggests that some etching occurred at the walls, enabling crystallographic faceting. Spiecker *et al.* (19) also reported faceting of pore walls for InP in acidic solution; the pore cross-sections were triangular but, as in the case of silicon, pore width increased with distance from the pore tip. In the present case of anodic anodization of InP in KOH, the etching process occurs only in a very small region near the pore tip and this region of reaction is constantly advancing. Therefore, the etching process does not delineate pore wall facets.

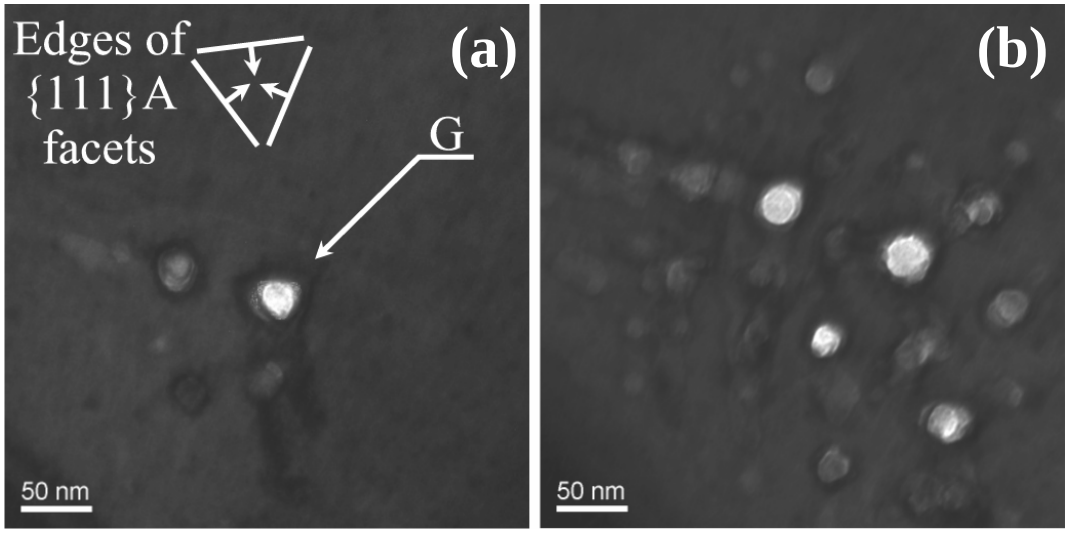


Fig. 3 TEM images, viewed along <111>B direction, of a $(01\bar{1})$ slice of InP. The cross-section in (a) passes through a pore close to its tip (at G) while the cross-section in (b) passes through pores far from their tips. The electrode had experienced a LPS from 0 to 0.44 V (SCE) in 5 mol dm^{-3} KOH at 2.5 mV s^{-1}. The FIB-milled InP slice is ~100 nm thick.

In III-V semiconductors the {111}B planes (*e.g.* the phosphorus planes in InP) are commonly found to be fast-etching both in electrochemical pore formation (19,20) and in wet etching of trenches (21). Therefore the direction of etching (*i.e.* the direction in which an etch front moves) is the <111>A direction. Gatos and Levine (22,23) have proposed a model for the {111} surfaces of III-V semiconductors with a zinc-blende structure. According to this model the etch rates of these surfaces are dependent on the relative reactivity of the terminating atoms. The {111}A plane is terminated by weakly reacting Group III (metallic) atoms and the {111}B plane is terminated by strongly reacting Group V (non-metallic) atoms. Subsequent work by Holt (24) on the behavior of these surfaces in InSb supports this model, showing a strong reactivity for the Sb and a weaker reactivity for the In. Research on the behavior of GaAs (25,26) and InP (27,28) in a range of etchants, such as Piranha (H_2SO_4-H_2O_2-H_2O mixtures) and bromine-methanol, has identified the {111}A planes as the slow etch planes that are revealed during chemical etching. Similar results for photo-electrochemical etching (29,30) and thermal decomposition (31) of InP have also shown the {111}A planes to be revealed due to the preferential removal of phosphorus.

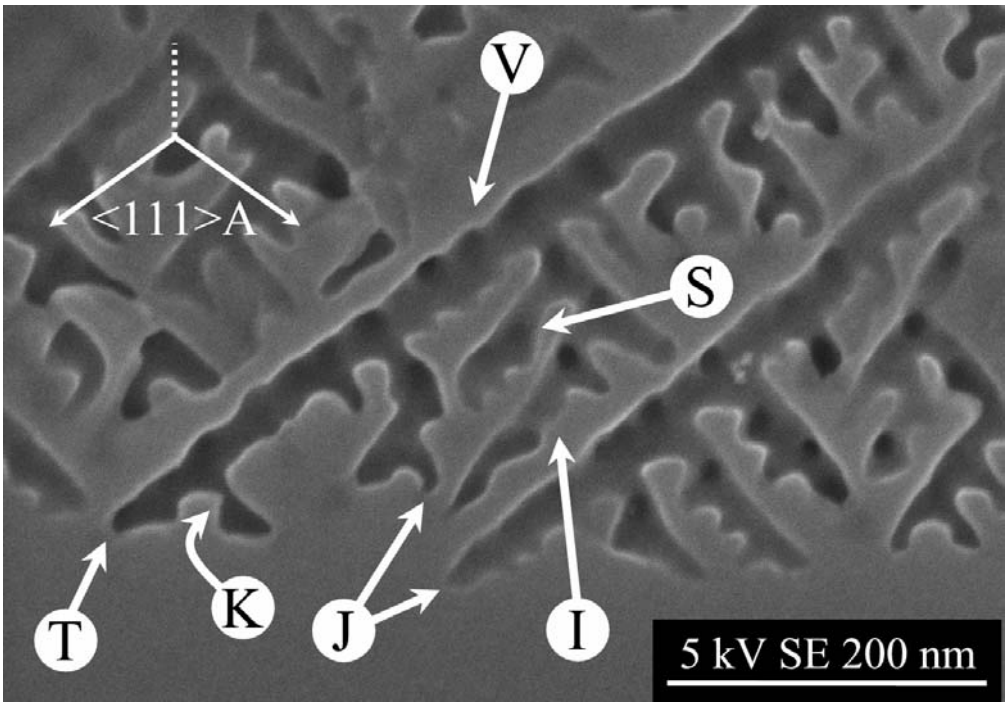


Fig. 4 Cross-sectional (011) SEM image of InP after an LPS from 0 to 0.383 V (SCE) in 5 mol dm^{-3} KOH at 2.5 mV s^{-1}.

Fig. 4 shows an SEM image of a (011) cross-section through a porous domain. Several interesting features of the pores can be observed in this image. As in Fig. 1 a primary pore can be seen at V. The pore has propagated along a <111>A direction and has rough but parallel edges. The parallel edges of this pore can be seen to end at a tip with a rounded point at T. Again, it can be seen that not all of the pores are exactly along the <111>A directions. This is especially the case where pores are branching from a primary pore and are in close proximity to regions that are depleted of carriers by the

presence of nearby pores. An example can be observed at S, where a pore has diverged from the primary pore at V. Also, at I a pore that is restricted by several neighboring pores (*e.g.* at J) has propagated into a bottle-neck resulting in a tapered shape. Again, at K restriction of the development of a branching pore at V has resulted in narrowing, presumably due to the proximity of other pores not visible in the micrograph. Despite this narrowing, the pore has later re-established a normal width.

Thus, pores propagate preferentially along the <111>A crystallographic directions and have both a characteristic pore width but may change direction and width so as to navigate past restricted regions. As shown in the next section, such behavior can be understood if it is assumed that the etching at the pore tip is controlled both by the high electric field (32), and by preferential etching of the {111}B phosphorus planes.

Pore Propagation Mechanism

Pore propagation is controlled both by the availability of charge carriers at the pore tips and by the strength of the electric field that enables transport of these carriers across the depletion layer surrounding the tips. The faster etch rate of InP {111}B faces is considered to be due to the full dangling bonds that extend from the surface phosphorus atoms (22,33). Near the pore tips the electric field is sufficiently high to enable substantial quantum tunneling of carriers (34) and these dangling bonds facilitate a higher etch rate resulting in the propagation of pore tips.

Modeling of the relationship between pore-tip shape and electric field in silicon by Zhang (32) showed that the electric field is dependent on the radius of curvature of the internal surface of a pore. He concluded that the electric field ξ at the surface is a function of the ratio of the radius of curvature r_o and the space-charge layer thickness x_{sc}, *i.e.* $\xi = \xi(r_o/x_{sc})$. Since a threshold electric field ξ_{th} must be attained for etching to occur, a corresponding threshold value Λ of r_o/x_{sc} must also exist. Thus, a reduction in x_{sc} corresponds to a reduction in the value of r_o at which the threshold values of Λ and ξ_{min} are attained.

A related mechanism of chemical etching has been described by MacFayden (35) where it was proposed that chemical etching progresses through the removal of the most loosely bound atoms from the crystal faces. In the case of III-V semiconductors, the {111}B atoms (e.g. phosphorus) are the most loosely bound. Atomic ledges on {111}A surfaces represent quasi-{111}B planes. Since these are the fast-etching planes, we propose that the ledges etch, revealing a fresh {111}A plane one monolayer beneath the original. Where such a {111}A plane has been revealed, there are no {111}B atoms remaining, but where a indium atom is removed from such a plane, a triangular-shaped void, one atom deep, surrounded by a ledge of {111}B phosphorus atoms is created. The phosphorus atoms on this ledge can then be etched, revealing loosely bound indium atoms which in turn can be easily etched to reveal a similar, but widened, triangular-shaped void in the {111}A surface surrounded by a ledge of {111}B phosphorus atoms. Therefore an indium vacancy in a {111}A surface allows a layer of atoms to etch quickly, in a zip-like fashion. This rapid etching occurs in a two-dimensional manner, outwards from the initial indium vacancy, exposing the next {111}A plane; the crystal can be considered to consist of layers like an onion that are removed one at a time.

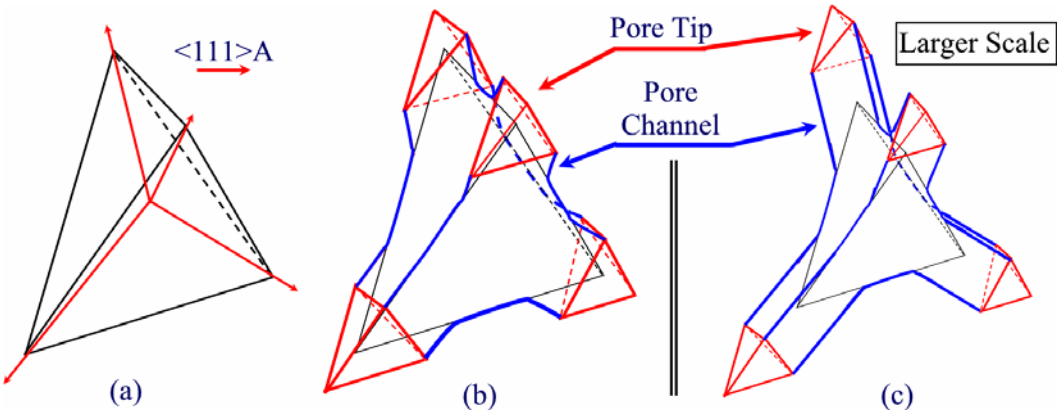


Fig. 5 Schematic representation of the widening of a hypothetical electrolyte-filled void in the bulk of the semiconductor. (a) Initially the etching leads to a tetrahedral shape. (b) As the void becomes larger, suitable conditions for etching continue to exist only at the vertices. Therefore (c) the void stops expanding while four pore tips grow outwards from the vertices along the <111>A directions.

Consider now an electrolyte-filled void in a semiconductor. At the semiconductor-electrolyte interface, under suitable conditions of electric field, carrier concentration and electrolyte composition, the zip-like propagation of etching described above will occur to reveal {111}A facets. These facets will enlarge until they meet, creating a tetrahedral shape as shown in Fig. 5a. As etching continues, the tetrahedron will increase in size. The electric field across the interface will vary with position on the surface of the tetrahedron, being greatest at the apexes and decreasing towards the centers of the faces. It follows that, as the tetrahedron grows, the electric field will eventually become too small to maintain etching near the centers of the four {111}A facets and etching will cease in that region while the remainder of the void will continue to etch. This situation is shown in Fig. 5b, where continued etching of void walls has resulted in the formation of four pore tips that point outwards from the vertices.

Zip-like etching will occur on the {111}A facets near the pore tips but the vertex of each tip will be maintained. If carriers are equally available at the three facets, etching progresses at the same rate at each facet with the result that the pore tip propagates along the <111>A direction. In the direction away from the tip, etching will occur until the electric field becomes too small to sustain it. In the wake of the propagation of the tip, a channel is therefore created, the walls of which do not etch because of the lack of a suitable electric field (see Fig. 5c).

To the rear of the growing tip structure, the availability of carriers is limited due to the proximity of the depletion region surrounding the void. Once the pore tip has progressed some distance from the starting point, carriers become available that allow the formation of a fourth <111>A facet to the rear of the propagating tip so that the tip structure now has three additional apexes (a total of four corresponding to the four <111>A directions as shown in Fig. 6a). Thus, the tip structure now has a tetrahedral shape which expands until the electric field near the centers of its facets becomes too small to sustain further etching while etching continues near the apexes (Fig. 6b). This results in the formation of tetrahedral tip structures at each of the four vertices, as depicted in Fig. 6c. Thus, a porous structure is formed by pores that propagate and branch along the <111>A directions.

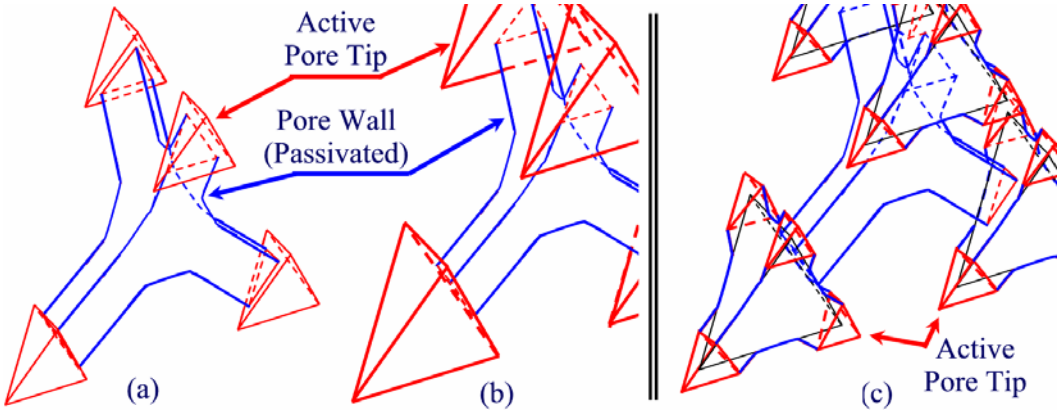


Fig. 6 Schematic representation of the widening of pore tips (a) after the tip has extended past the depletion region of the void from which it originated, followed by (b) the expansion of these tips into tetrahedral voids until their radii of curvature match the characteristic radius of curvature. This expansion of the pore tips leads (c) to branching of the pores along the <111>A directions.

As shown in Fig. 5c, a pore propagates along the <111>A direction because the {111}A facets near the tip are etched at equal rates when the two factors that enable etching (electric field and carrier availability) are present to equal degrees at all three {111}A facets.

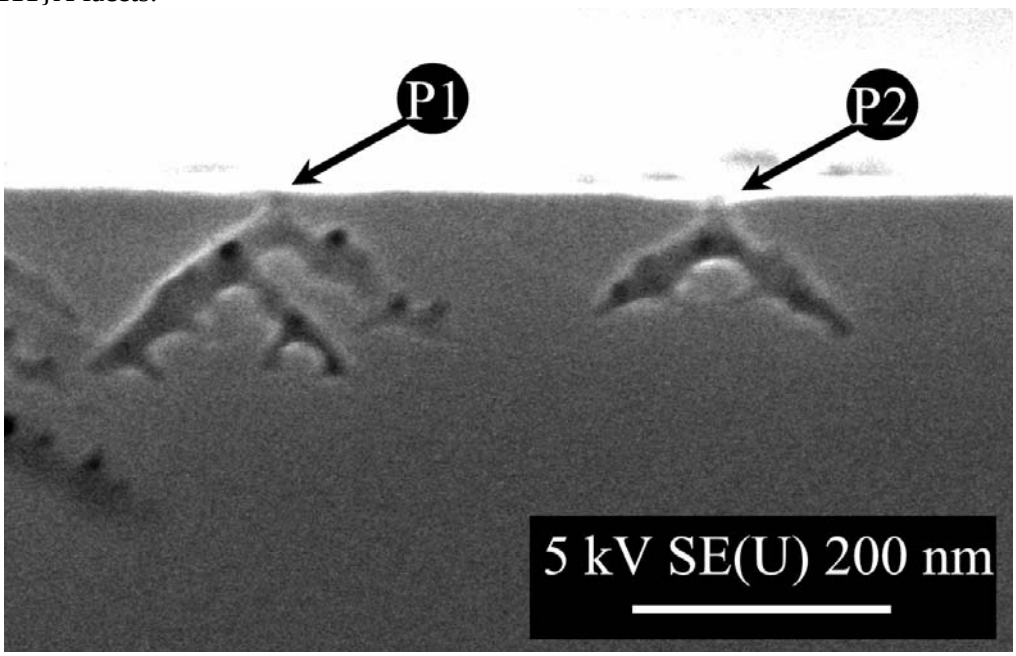


Fig. 7 Cross-sectional (011) SEM image showing pits at P1 and P2 that connect the surface to two primary pores. The n-InP electrode was anodized in 5 mol dm^{-3} KOH by a LPS from 0 to 0.245 V (SCE) at 2.5 mV s^{-1}.

If either of these factors is diminished at any of the three tip facets, the etch rate at that facet decreases, causing the propagation of the pore tip to deviate away from that facet. Thus, when a pore tip is close to an existing pore, the absence of carriers due to the

overlapping of the depletion layers around the pore results in the pore tip been redirected away from it. The outcome from such a process can be seen at S in Fig. 4 where the pore tip has veered away from the pre-existing pore channel at V.

A similar situation arises at the surface pits. The cross-section in Fig. 7 shows two sets of pores and the surface pits from which they originate. Such pits (channels) along the $[\bar{1}00]$ direction connect the surface (electrolyte) to the underlying porous domains, through the near-surface layer as depicted in Fig. 8. Once a surface pit has formed, its preferred shape is, like that of any void, a tetrahedron. However, carriers are available only by tunneling through the depletion layer at the surface and this can occur only at small angles to the surface normal as shown at x and y in Fig. 8b. Thus, the surface pit is initially constrained to grow only along the normal to the surface causing the formation of a very narrow channel as shown in Fig. 8c. Once a channel has grown a certain distance through the depletion layer, the availability of carriers at the sides of the channel tip allows the formation of tetrahedrally oriented facets as shown in Fig. 8c and 8d. This truncated tetrahedron continues to expand (Fig. 8e) until the electric field near the centers of its facets becomes insufficient to sustain etching while etching continues near the apexes. This results in the formation of two primary pores as shown in Fig. 8f. As observed in Fig. 7, this process results in the channels (shown at P1 and P2 in Fig. 7) that form pits in the surface layer along the $[\bar{1}00]$ direction leading to the formation of two primary pores at each pit. Similarly, the channel formed during the restricted growth of the pore at K in Fig. 4 is due to the propagation of a tip through a similarly wide depletion region that exists between two pre-existing pores that are not parallel to the propagation direction of the pore tip.

Effect of Carrier Concentration on Porous Domain Dimensions

The carrier concentration of the InP has a major effect on the electrochemical process resulting in changes in the magnitude and position of current peaks and in the overall shape of linear sweep voltammograms (LSVs) (11).

Table 1 shows how several porous layer parameters vary with carrier concentration for three highly doped InP electrodes. With increasing carrier concentration, surface pit diameter increases and both the near-surface layer thickness and the pore width decrease. Although the variation of these parameters is not large, this is a very interesting result since it suggests a relationship between the mechanisms that determine, respectively, the thickness of the near-surface layer and the pore width while also suggesting that the surface pit diameter and the pore width are not directly related.

To explain the variation of the parameters in Table 1, it is useful to consider the width x_{sc} of the depletion layer at the semiconductor solution interface. For a given potential difference across the interface, the depletion layer decreases with increasing carrier concentration. This variation in x_{sc} can help explain the results of Table 1 because the pore growth mechanism is dependant on the tunneling of carriers across the depletion layer. Thus, as x_{sc} decreases, the widths of the near-surface layer, inter-pore walls and pores, respectively, should also decrease. The explanation for the observed increase in pit diameter with increasing carrier concentration is not obvious. It may simply be due to a geometrical effect that causes the surface pits to widen as the thickness of the near-surface layer decreases.

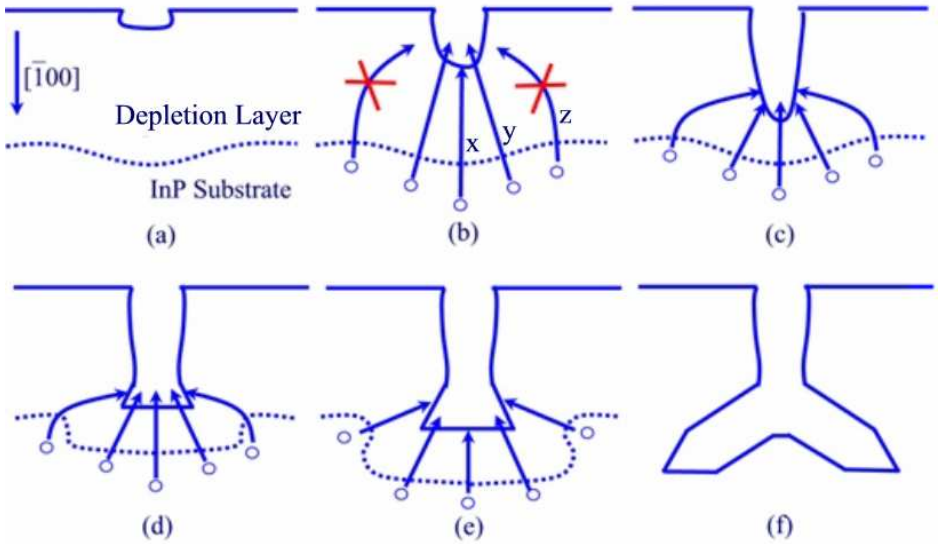


Fig. 8 Schematic representation of the progression of etching from (a) a pit in the surface. (b) The lower surfaces of this pit etch vertically downwards due to decreasing availability of carriers with increasing angle to the surface normal (from x to z). This etching results in the formation (c) of a long, narrow channel in the [$\bar{1}$00] direction. Once the channel is deep enough, the availability of carriers to the sides allows some lateral etching. (d) This etching widens the end of the channel into (e) a truncated tetrahedral void that produces (f) two primary pores when the void is sufficiently large.

The pore wall and near-surface layer thicknesses are influenced by the redirection of pore growth away from regions of limited carrier availability. As discussed earlier, this process occurs where the depletion layers of two neighboring regions overlap. The pores etch faster in directions where carriers are available, with the result that tips propagate away from, or around, existing pores. Therefore, at higher carrier concentrations the depletion layer is thinner and consequently pores can grow much closer together, decreasing the thickness of both the inter-pore walls and the near-surface layer.

Table 1 Variation, due to carrier concentration of InP, of average values for three porous layer parameters: surface pit diameter, near-surface layer thickness and pore width.

Carrier Concentration / 10^{18} cm^{-3}	Surface-Pit Diameter / nm	Near-Surface Layer-Thickness / nm	Pore Width / nm
3.4	14	45	30
5.3	17	39	28
6.7	22	34	19

As explained earlier, a minimum electric field ξ_{min} is required for quantum tunneling across the depletion layer at the pore tip to occur and the value of ξ_{min} is dependent on the ratio r_o/x_{sc}. Since a threshold electric field ξ_{th} must be attained for etching to take place, a

corresponding limiting value Λ of r_o/x_{sc} also exists. Therefore a decrease in x_{sc} must be matched by a proportionate decrease in r_o so as to maintain the value of Λ. Since the value of x_{sc} at a given potential decreases with increasing carrier concentration, the radius of curvature of the pore must also decrease resulting in a decrease in pore width.

Conclusions

Observations of pore cross-sections, using SEM and TEM images, suggest that pore tips are pyramidal in shape with {111}A internal faces. Despite the tip shape, the pore cross-sections are round and the pore width is constant with respect to distance from the tip, *i.e.* the pores are cylindrical in shape. The {111}A faces near the tip are revealed due to fast etching of loosely bound {111}B phosphorus atoms. This process results in removal of planes of atoms parallel to the {111}A facets beginning with an indium vacancy in a {111}A face. A vertex is therefore maintained where the three {111}A facets, intersect; this, in turn, maintains the electric field near the tip due to the high surface curvature in this region. To the rear of the tip, the electric field decreases below the threshold value required for etching and the locus of the threshold electric field on the {111}A facets is such that the resulting pore cross-section is approximately circular.

Where the availability of carriers is reduced near one of the facets at a pore tip, etching is reduced at the facet causing pore growth to deviate from the <111>A direction. This also results in changes in the shape of a tip and the channel that is left in its wake. Such reductions in the availability of carriers can occur where the depletion region surrounding the tip overlaps another region that is depleted of carriers, *e.g.* during the formation of a pit in the electrode surface or when a pore tip is close to an existing pore or to the near-surface layer.

References

1. R. L. Smith and S. D. Collins, *J. Appl. Phys.*, **71**, 8 (1992).
2. S. Langa, J. Carstensen, M. Christophersen, H. Föll, and I. M. Tiginyanu, *Appl. Phys. Lett.*, **78**, 1074 (2001).
3. G. Oskam, A. Natarajan, P. C. Searson, and F. M. Ross, *Appl. Surf. Sci*., **119,** 160 (1997).
4. S. Langa, J. Carstensen, I. M. Tiginyanu, M. Christophersen, and H. Föll, *Electrochem. Solid-State Lett.*, **4**, G50 (2001).
5. S. Langa, I. M. Tiginyanu, J. Carstensen, M. Christophersen, and H. Föll, *Electrochem. Solid-State Lett.*, **3**, 514 (2000).
6. P. Schmuki, J. Fraser, C. M. Vitus, M. J. Graham, H. S. Isaacs, *J. Electrochem. Soc.*, **143,** 3316 (1996).
7. P. Schmuki, D. J. Lockwood, J. Fraser, M. J. Graham, H. S. Isaacs, *Mater. Res. Soc. Symp. Proc.*, **431,** 439 (1996).
8. M. Christopherson, J. Cartensen, A. Feuerhake, and H. Föll, *Mater. Sci. Eng. B,* **69,** 70, 194 (2000).
9. S. Rönnebeck, J. Carstensen, S. Ottow, and H. Föll, *Electrochem. Solid-State Lett.*, **2**, 126 (1999).
10. P. Schmuki, L. E. Erickson, D. J. Lockwood, J. W. Fraser, G. Champion, H. J. Labbé, *Appl. Phys. Lett.*, **72**, 1039 (1998).

11. R. Lynch, C. O'Dwyer, D. Sutton, S. Newcomb, and D. N. Buckley, *ECS Trans.*, **6**, 355 (2007).
12. C. O'Dwyer, D. N. Buckley, D. Sutton, M. Serantoni, and S. B. Newcomb, *J. Electrochem. Soc.*, **154**, H78 (2007).
13. D. N. Buckley, C. O'Dwyer, R. Lynch, et al., Proceedings of the 41st State-of-the-Art Program on Compound Semiconductors, PV 2004-05, p.103 (ECS, 2004).
14. C. O'Dwyer, D. N. Buckley, D. Sutton, and S. B. Newcomb, *J. Electrochem. Soc.*, **153**, G1039 (2006).
15. R. Lynch, M. Dornhege, P. Sánchez-Bodega, H. H. Rotermund, and D. N. Buckley, *ECS Trans.*, **6**, 331 (2007).
16. R. Lynch, C. O'Dwyer, D. N. Buckley, D. Sutton, and S. B. Newcomb, *ECS Trans.*, **2**, 131 (2006).
17. L. A. Giannuzzi and F. A. Stevie, *Micron.*, **30**, 197 (1999).
18. T. Osaka, K. Osgasawara, and S. Nakahara, *J. Electrochem. Soc.*, **144**, 3750 (1991).
19. E. Spiecker, M. Rudel, W. Jäger, M. Leisner and H. Föll, *phys. stat. sol. (a),* **202,** 2950 (2005).
20. S. Langa, J. Carstensen, I. M. Tiginyanu, M. Christophersen, and H. Föll. *Electrochem. Solid-State Lett.,* **5**, C14 (2002).
21. M. Kappelt and D. Bimberg, *J. Electrochem. Soc.*, **143**, 3271 (1996).
22. H. C. Gatos and M. J. Lavine, *J. Electrochem. Soc.*, **107**, 427 (1960).
23. H. C. Gatos, *J. Appl. Phys.*, **32**, 1232 (1961).
24. D. B. Holt, *J. Appl. Phys.*, **31**, 2231 (1960).
25. Y. Tarui, Y. Komiya and Y. Harada, *J. Electrochem. Soc.*, **118**, 118 (1971); S. Iida and K. Ito, *J. Electrochem. Soc.*, **118**, 768 (1971).
26. S. Adachi and K. Oe, *J. Electrochem. Soc.*, **130**, 2427 (1983).
27. P. H. L. Notten, *J. Electrochem. Soc.*, **138**, 243 (1991).
28. I. E. Vermeir, W. P. Fomes, and P. van Daele, *J. Electrochem. Soc.*, **142**, 3226 (1995).
29. D. Soltz and L. Cescato, *J. Electrochem. Soc.*, **143**, 2815 (1996).
30. M. M. Carrabba, N. M. Nguyen, and R. D. Rauh, *J. Electrochem. Soc.*, **134**, 1855 (1987).
31. S. N. G. Chu, C. M. Jodlauk, and W. D. Johnston, Jr., *J. Electrochem. Soc.*, **130**, 2399 (1983).
32. X. G. Zhang, *J. Electrochem. Soc.*, **138**, 3750 (1991).
33. M. Nishida, *J. Phys. C*, **12**, 535 (1981).
34. X. G. Zhang, *J. Electrochem. Soc.*, **151**, C69 (2004).
35. D. N. MacFayden, *J. Electrochem. Soc.*, **130**, 1934 (1983).